

# Lawrence Berkeley National Laboratory

## LBL Publications

### Title

Magnetic MoS<sub>2</sub> Interface Monolayer on a CdS Nanowire by Cation Exchange

### Permalink

<https://escholarship.org/uc/item/7jh8r06n>

### Journal

The Journal of Physical Chemistry C, 120(40)

### ISSN

1932-7447

### Authors

Tan, Chih-Shan  
Lu, Yu-Jung  
Chen, Chun-Chi  
et al.

### Publication Date

2016-10-13

### DOI

10.1021/acs.jpcc.6b07679

Peer reviewed

# Magnetic MoS<sub>2</sub> Interface Monolayer on a CdS Nanowire by Cation Exchange

[Chih-Shan Tan](#)<sup>†</sup>, [Yu-Jung Lu](#)<sup>‡</sup>, [Chun-Chi Chen](#)<sup>§</sup>, [Pei-Hsuan Liu](#)<sup>†</sup>, [Shangjr Gwo](#)<sup>‡</sup>, [Guang-Yu Guo](#)<sup>||,⊥</sup>,  
and [Lih-Juann Chen](#)<sup>†</sup>

<sup>†</sup> Department of Materials Science and Engineering, National Tsing Hua University, Hsinchu, Taiwan 30043, R.O.C.

<sup>‡</sup> Department of Physics, National Tsing Hua University, Hsinchu, Taiwan 30043, R.O.C.

<sup>§</sup> National Nano Device Laboratories, National Applied Research Laboratories, 26, Prosperity Road I, Hsinchu, Taiwan 30078, R.O.C.

<sup>||</sup> Department of Physics, National Taiwan University, Taipei, Taiwan 10617, R.O.C.

<sup>⊥</sup> Physics Division, National Center for Theoretical Sciences, Hsinchu, Taiwan 30078, R.O.C.

*J. Phys. Chem. C*, **2016**, *120* (40), pp 23055–23060

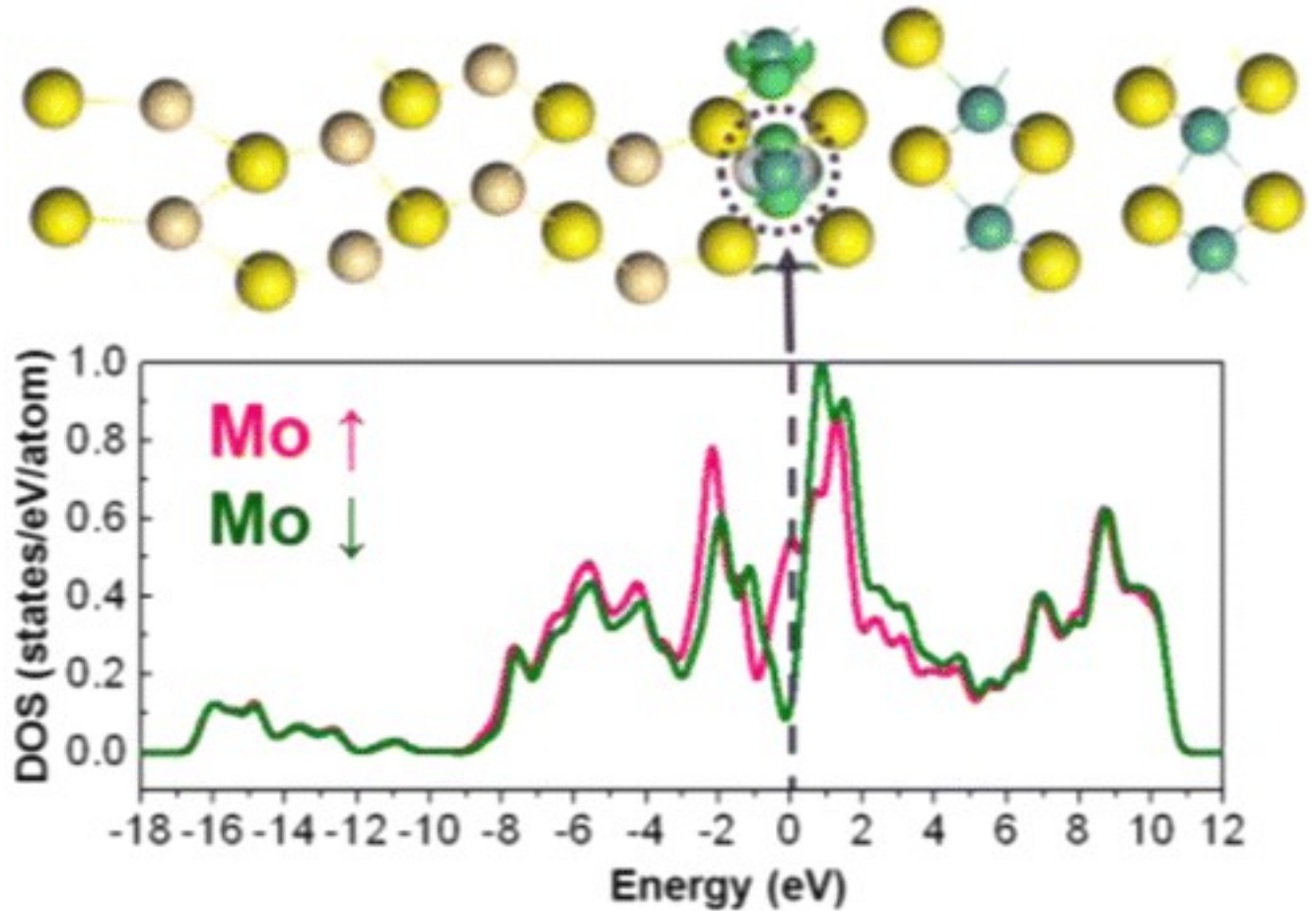
DOI: 10.1021/acs.jpcc.6b07679

Publication Date (Web): October 3, 2016

\*E-mail: [gyguo@phys.ntu.edu.tw](mailto:gyguo@phys.ntu.edu.tw), \*E-mail: [ljchen@mx.nthu.edu.tw](mailto:ljchen@mx.nthu.edu.tw).

•

## Abstract



MoS<sub>2</sub> atomic layers have recently attracted much interest because of their two-dimensional structure as well as tunable optical, electrical, and mechanical properties for next-generation electronic and electro-optical devices. Here we have achieved facile fabrication of MoS<sub>2</sub> thin films on CdS nanowires by cation exchange in solution at room temperature and importantly observed their extraordinary magnetic properties. We establish the atomic structure of the MoS<sub>2</sub>/CdS heterostructure by taking atomic images of the MoS<sub>2</sub>/CdS interface as well as performing first-principles density functional geometry optimizations and scanning transmission electron microscopy annular dark field image simulations. Furthermore, our first-principles density functional calculations for the MoS<sub>2</sub>/CdS heterostructure reveal that the magnetism in the MoS<sub>2</sub>/CdS heterostructure stems from the ferromagnetic MoS<sub>2</sub> monolayer next to the MoS<sub>2</sub>/CdS interface. The ferromagnetism is attributed to the partial occupation of the Mo  $d_{x^2-y^2}/d_{xy}$  conduction band in the interfacial MoS<sub>2</sub> monolayer caused by the mixed covalent–ionic bonding among the MoS<sub>2</sub> and CdS monolayers near the MoS<sub>2</sub>/CdS interface. These findings of the ferromagnetic MoS<sub>2</sub> monolayer with large spin polarization at the MoS<sub>2</sub>/semiconductor interface suggest a new route for fabrication of the transition

metal dichalcogenide-based magnetic semiconductor multilayers for applications in spintronic devices.

## Introduction

Transition metal dichalcogenide (TMD) monolayers,[\(1-4\)](#) especially those of molybdenum disulfide ( $\text{MoS}_2$ ),[\(5-8\)](#) have recently attracted much interest because of their controllable optical, electrical, and mechanical properties for next-generation devices. Bulk  $\text{MoS}_2$  consists of sandwichlike S–Mo–S monolayers in which each Mo atom is connected to six S atoms with covalent bonds. The sandwich  $\text{MoS}_2$  monolayers are bound together by weak van der Waals forces. The band structure of  $\text{MoS}_2$  undergoes a remarkable change from an indirect band gap of  $\sim 1.2$  eV in the bulk to a direct one of  $\sim 1.8$  eV for a single monolayer.[\(9\)](#)  $\text{MoS}_2$  nanowires exhibit excellent electrochemical performance in lithium ion batteries.[\(10\)](#) Recent researches have been focused on the excellent optical and electrical properties of  $\text{MoS}_2$ , and some are also related to the novel magnetic properties of  $\text{MoS}_2$ . For example, it has been reported that the valley magnetic moment of the  $\text{MoS}_2$  monolayer could be electrically tuned[\(11\)](#) and that zigzag and armchair nanoribbons of  $\text{MoS}_2$  could exhibit metallic (ferromagnetic) and semiconducting (nonmagnetic) behavior.[\(12-15\)](#) It has also been predicted that large spin polarization could be induced in the interfacial  $\text{MoS}_2$  monolayer in the ferromagnetic  $\text{Fe}_4\text{N}/\text{MoS}_2$  bilayer because of the magnetic proximity effect.[\(16\)](#) Spintronic devices are being developed with vigorous efforts,[\(17, 18\)](#) and a spin transistor[\(5, 19, 20\)](#) is believed to be the most promising next-generation spintronic device.

Although a large amount of research has been directed at the formation of  $\text{MoS}_2$  films with atomic thickness, scarce attention has been paid to the process of formation of  $\text{MoS}_2$  films and the bonding and physical properties of the  $\text{MoS}_2$  layer with other semiconductor materials. Here we use cation exchange to grow epitaxial  $\text{MoS}_2$  layers on the surface of CdS nanowires (NWs) at room temperature. Remarkably, we discover that the  $\text{MoS}_2/\text{CdS}$  heterostructures are ferromagnetic. Our first-principles density functional calculations reveal that the magnetism originates from the  $\text{MoS}_2$  monolayer at the  $\text{MoS}_2/\text{CdS}$  interface with a spin magnetic moment of  $\sim 0.5 \mu_B$  on the Mo atom and a large spin polarization ( $\sim 63\%$ ) of the electronic states at the Fermi level. The occurrence of magnetization in the interfacial  $\text{MoS}_2$  monolayer is attributed to the Mo cation sharing of its d electron with the Cd cation. As  $\text{MoS}_2$  is considered to be an excellent material for transistors,[\(5\)](#) the findings presented here of the itinerant magnetism in the  $\text{MoS}_2$  monolayer at the  $\text{MoS}_2$ /semiconductor

interface may reveal a new opportunity for the fabrication of the magnetic two-dimensional (2D) TMD materials on three-dimensional (3D) nanostructures for application in spin transistors and other semiconductor spintronic devices.

## Experimental and Computational Methods

### CdS NW Synthesis

CdS NWs were grown by using the method reported in ref [21](#).

### Cation Exchange Transformation

CdS NWs were dipped into ethylene glycol (99.5%, Sigma-Aldrich) containing 0.1 M molybdenum(V) chloride (Alfa Aesar, 99.6%) at room temperature. After 6 h, the CdS NWs completely transformed into MoS<sub>2</sub> NWs. We can change the MoS<sub>2</sub> shell thickness by varying the reaction time.

### Instrumentation

FE-SEM images were obtained using a FEI Helios 1200+ FE-SEM instrument. TEM images were recorded using JEOL ARM200F and 2010F electron microscopes. Raman measurements were taken with a Horiba Jobin Yvon, LABRAM HR 800 UV instrument. The magnetic measurements were taken using a SQUID instrument (MPMS XL-7).

### Scanning Transmission Electron Microscopy (STEM) Image Simulations

Scanning transmission electron microscopy annular dark field (STEM-ADF) image simulations of the model MoS<sub>2</sub>/CdS heterostructures were performed with QSTEM.[\(22\)](#) The input parameters were set according to our experimental conditions, including the probe size, the convergence angle, and the acceptance angle of the ADF detector. To enhance the contrast of the sulfur atoms, the medium-range ADF mode was selected instead of the high-angle ADF mode by proper adjustment of the camera length. The detector angle is at a pivot condition (with 20–60 mrad) between the medium-range ADF mode and the high-angle ADF mode.

### Density Functional Calculations

Several initial atomic models of the MoS<sub>2</sub>/CdS heterostructure were constructed by different combinations of MoS<sub>2</sub> (00 $\bar{2}$ ) and CdS (002) thin layers. First-principles geometry optimizations for these initial atomic models of the MoS<sub>2</sub>/CdS heterostructure were performed on the basis of density functional theory (DFT) with the generalized gradient approximation (GGA) of the Perdew–Burke–Ernzerhof form.[\(23\)](#) The optimized MoS<sub>2</sub>/CdS heterostructure models were then used to simulate the STEM-ADF image. The atomic model that produces the image best fitting to the real STEM-ADF

image is displayed in [Figure 1](#), and also used in the subsequent GGA calculations of the electronic and magnetic properties of the MoS<sub>2</sub>/CdS heterostructure. First-principles DFT-GGA calculations were performed by using the plane wave norm conserving pseudopotential method, as implemented in the Cambridge Serial Total Energy Package (CASTEP). The plane wave basis set cutoff energy is 720 eV. We used a fine k-point mesh of 5 × 8 × 1 for the Brillouin zone integration throughout.

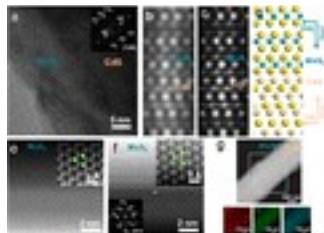


Figure 1. Heterojunction area analysis of MoS<sub>2</sub>/CdS NWs after cation exchange. (a) High-resolution TEM image of the MoS<sub>2</sub>/CdS heterostructure at the junction area (after reaction for 3 min). The inset is the corresponding FFT pattern. (b) STEM-ADF image of the MoS<sub>2</sub>/CdS heterostructure (after reaction for 3 min). (c) Simulated STEM-ADF image of the MoS<sub>2</sub>/CdS heterostructure. (d) Atomic model of the MoS<sub>2</sub>/CdS junction. (e) STEM-ADF image of the MoS<sub>2</sub> region (after reaction for 3 min). The top right inset is the magnified image of panel e. (f) STEM-ABF image of the MoS<sub>2</sub> region (after reaction for 3 min). The top right and bottom left insets are the magnified image and FFT pattern, respectively. The blue and yellow dots represent Mo and S atoms, respectively. (g) STEM image and EDS mapping of CdS NW after Mo ion exchange for 10 min.

## Results and Discussion

Cation exchange is an ionic reaction process for III–V and II–VI semiconductors and metal–organic frameworks for changing the components and structures<sup>(24-26)</sup> as well as a convenient method for fabricating optical and electrical devices.<sup>(27)</sup> In a previous work, ion exchange was used to convert CdS nanowire templates to Cu<sub>2</sub>S/Ag<sub>2</sub>S superlattice p/n heterojunction NWs due to ionic bonding preferences between the different cation and anion.<sup>(21)</sup> In the work presented here, MoS<sub>2</sub> layers were grown on CdS nanowires by cation exchange and the magnetic properties of MoS<sub>2</sub> (shell)/CdS (core) NWs were explored. CdS NWs were dipped in a molybdenum ionic solution at room temperature (RT), and atomic layers of MoS<sub>2</sub> were grown on CdS NWs. By control of the reaction time, different thicknesses, from one atomic layer to tens of atomic layers, of MoS<sub>2</sub> can be grown on CdS NW as a shell by cation exchange. Finally, the CdS NWs were completely transformed to MoS<sub>2</sub> NWs after several hours.

The ex situ Raman spectra of cation exchange from CdS NWs to MoS<sub>2</sub> NWs with different reaction times of up to 6 h were monitored. Via identification of the E<sub>2g</sub><sup>1</sup> (in-plane vibration) and A<sub>1g</sub> (out of plane) peaks, the gradual formation of MoS<sub>2</sub> structure with increasing reaction time can be inferred ([Figure S1](#) and ref [28](#)). The data exhibit clearly the 302 cm<sup>-1</sup> peak, which is the first-order longitudinal optical mode (1LO) of CdS. After cation exchange, the CdS 1LO peak shifts gradually with strain and eventually disappears. On the other hand, the magnitudes of E<sub>2g</sub><sup>1</sup> and A<sub>1g</sub> signals of MoS<sub>2</sub> increase gradually. It is difficult to identify the actual location of the E<sub>2g</sub><sup>1</sup> peak at 376 cm<sup>-1</sup> near the CdS peaks until the completion of the reaction. The A<sub>1g</sub> peaks during the cation exchange from CdS to MoS<sub>2</sub> NWs are at 408 cm<sup>-1</sup> (2 min), 405 cm<sup>-1</sup> (3 min), 407 cm<sup>-1</sup> (4 min), 407 cm<sup>-1</sup> (5 min), 405 cm<sup>-1</sup> (10 min), 407 cm<sup>-1</sup> (30 min), 407 cm<sup>-1</sup> (1 h), 406 cm<sup>-1</sup> (2 h), and 406 cm<sup>-1</sup> (6 h). It indicates that the stress and strain are varied with reaction time and MoS<sub>2</sub> thickness. SEM images are shown in [Figure S2](#). Bright field transmission electron microscopy (BF-TEM) and scanning transmission electron microscopy–energy dispersive spectroscopy (STEM–EDS) were performed to obtain structural information about the MoS<sub>2</sub>/CdS interface. We analyzed the MoS<sub>2</sub> on the CdS NW surface after cation exchange reaction for 3–10 min by BF-TEM ([Figure 1a](#)). After STEM imaging and EDS mapping of Mo, Cd, and S ([Figure 1g](#)), the core–shell structure of CdS–MoS<sub>2</sub> is evident. The scanning transmission electron microscopy annular dark field (STEM-ADF) image ([Figure 1b](#)) further reveals that MoS<sub>2</sub> (002̄) is connected with CdS (002) ([Figure 1b](#)). The STEM-ADF image matches rather well with the simulated image ([Figure 1c](#)) using the atomic model described below ([Figure 1d](#)). We built many atomic models for the MoS<sub>2</sub>/CdS heterostructure and then performed first-principles geometry optimization calculations for these models that were used in the STEM-ADF image simulations by QSTEM.[\(22\)](#) The MoS<sub>2</sub>/CdS heterostructure shown in [Figure 1d](#) is the heterostructure model with the simulated STEM-ADF image ([Figure 1c](#)) fitted best to the real STEM-ADF image ([Figure 1b](#)). From the STEM-ADF ([Figure 1e](#)) and ABF ([Figure 1f](#)) images, with magnified images as insets, the hexagonal structure of MoS<sub>2</sub> along the [001] direction is evident. Both CdS and MoS<sub>2</sub> are of a hexagonal closely packed (hcp) crystal structure with different lattice parameters. For CdS,  $a = b = 0.413$  nm and  $c = 0.671$  nm. For MoS<sub>2</sub>,  $a = b = 0.316$  nm and  $c = 1.229$  nm. Consequently, for growth of (002̄) MoS<sub>2</sub> on (002) CdS, the lattice mismatch between CdS and MoS<sub>2</sub> would be as high as 23%. On the other hand, no dislocations were observed at the interface. The absence of misfit dislocations is attributed to the difficulty in nucleation of dislocations in nanostructures.[\(29, 30\)](#)

The hysteresis loops of CdS NWs and MoS<sub>2</sub>/CdS NWs have been obtained by a superconducting quantum interference device (SQUID) ([Figure 2a–c](#) and [Figure S2](#)) with different cation exchange

time (3 s, 6 s, 9 s, 12 s, 1 min, 5 min, 10 min, 30 min, 60 min, 2 h, and 6 h). After cation exchange for 6 h, CdS NWs ( $M_s = 1.135 \times 10^{-3}$  emu/g, and  $H_{c\perp} = 215.8$  Oe) transform completely to MoS<sub>2</sub>NWs ( $M_s = 5.53 \times 10^{-3}$  emu/g, and  $H_{c\perp} = 149.9$  Oe), and both of them are ferromagnetic. Obviously, growth for 1 min of MoS<sub>2</sub> on CdS NWs leads to the strongest saturation magnetization intensity. In addition, the low-temperature ( $T = 4$  K) hysteresis loop shows a coercivity ( $H_{c\perp} = 973$  Oe) and saturation magnetization intensity ( $M_s = 4.43 \times 10^{-2}$  emu/g) (Figure S3) higher than the coercivity ( $H_{c\perp} = 200$  Oe) and saturation magnetization intensity ( $M_s = 1.3 \times 10^{-2}$  emu/g) at room temperature. Figure 2d reveals that the  $M_s$  decreases with MoS<sub>2</sub> thickness.

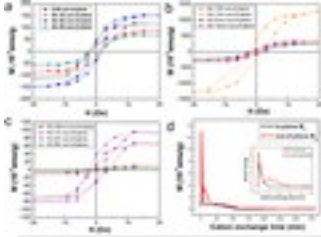


Figure 2. Magnetic measurements of MoS<sub>2</sub>/CdS NWs. (a–c) Hysteresis loops of CdS NWs and MoS<sub>2</sub>/CdS NWs in the out-of-plane direction.  $M$  is magnetization, and  $H$  is applied field. (d) Saturation magnetization of MoS<sub>2</sub>/CdS NWs as a function of cation exchange time.

For further exploration of the origin and nature of the observed magnetization ( $M$ ), the knowledge of the electronic structure and atom-resolved magnetization in the MoS<sub>2</sub>/CdS heterostructure is essential. Therefore, we have performed self-consistent spin-polarized electronic structure calculations within the DFT-GGA.<sup>(23)</sup> The atomic model shown in Figure 1d, which generates the simulated STEM-ADF image (Figure 1c) that fits best to the real STEM ADF image (Figure 1b), has been used in the DFT-GGA calculation.

A previous DFT-GGA calculation shows that free-standing few-layer thin films of MoS<sub>2</sub> have no magnetic moment.<sup>(31)</sup> In contrast, this calculation shows that the MoS<sub>2</sub> monolayer next to the CdS substrate becomes ferromagnetic with a Mo magnetic moment ( $m_s$ ) of  $\sim 0.5 \mu_B$  and a large electronic state spin polarization ( $P$ ) of  $\sim 63\%$  at the Fermi level (Figure 3d). Spin polarization  $P = (N_{\uparrow} - N_{\downarrow}) / (N_{\uparrow} + N_{\downarrow})$ , where  $N_{\uparrow}$  and  $N_{\downarrow}$  are the spin-up and spin-down densities of states (DOSs) at the Fermi level (EF), respectively. The Mo magnetic moment and spin polarization are greatly reduced in the second ( $m_s = 0.01 \mu_B$ , and  $P = 15\%$ ) and third ( $m_s = 0.00 \mu_B$ , and  $P = 2\%$ ) monolayers of MoS<sub>2</sub> away from the interface, as demonstrated by the calculated Mo-decomposed spin-resolved densities of states (DOSs) displayed in Figure 3d (and also Figure S5). Experimentally, the thinner MoS<sub>2</sub> layers are observed to possess a higher magnetization ( $M_s$ ), and this is consistent with the results of the



DFT calculation. Clearly, both experimental data and DFT calculation indicate that the interfacial MoS<sub>2</sub> layer has the predominant contribution to the MoS<sub>2</sub>/CdS magnetic properties.

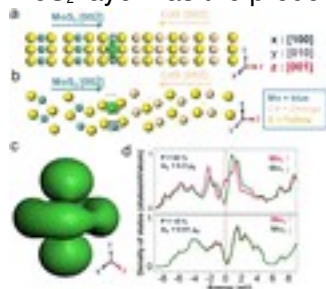


Figure 3. Atomic structure and DFT calculation of the magnetic property of the MoS<sub>2</sub>/CdS heterostructure. Atomic models of the MoS<sub>2</sub>/CdS heterostructure with MoS<sub>2</sub> (002) connecting with CdS (002) along (a) [010] and (b) [110] zone axes. The calculated spin density is concentrated at the first layer of Mo atoms from the junction. (c) Shape (isosurface) of the spin density of the Mo atom on the interfacial MoS<sub>2</sub> monolayer. (d) Spin-resolved DOSs of the Mo atoms on the first and second layers of the interface (top and bottom panels). The red dashed line indicates the Fermi level.

The observed dependence of magnetization on the thickness of the MoS<sub>2</sub> layer on the CdS NW is consistent with the theoretical finding of the magnetism in the MoS<sub>2</sub> monolayer at the MoS<sub>2</sub>/CdS interface as revealed by our atomic model (Figures 1d and 3a). Raman peaks ( $E_{2g}^1$  and  $A_{1g}$ ) of the MoS<sub>2</sub> layer (Figure S1) are clearly seen after cation exchange for 2 min, indicating that the quality of the MoS<sub>2</sub> structure improves as the thickness increases. Indeed, our Raman results show that our MoS<sub>2</sub> layer has a fine 2D structure on the CdS NW with clear in-plane and out-of-plane vibration modes. This explains that the few-layer thick MoS<sub>2</sub> structures have a poor magnetic property. For example, for very few-layer thick MoS<sub>2</sub> films on CdS NWs [3 s (0.5 layer), 6 s (1 layer), 9 s (1.5 layers), and 12 s (2 layers)], the  $M_s$  values are lower than that for 5 nm (reaction for 5 min) thick MoS<sub>2</sub> on CdS NWs. For MoS<sub>2</sub> with an improved structure, the interfacial magnetism starts to dominate the magnetic properties. On the other hand, for MoS<sub>2</sub> shells of >5 nm on CdS NWs, the influence of the interfacial magnetism is weakened. As a result, the magnetization decreases with an increase in MoS<sub>2</sub> thickness. Overall, as the CdS NW gradually transforms to the MoS<sub>2</sub> NW, the maximal magnetization moment ( $M_{max}$  or  $M_s$ ) increases first sharply with the formation of a thin shell of MoS<sub>2</sub> and then decreases rapidly. This phenomenon is similar to the variation of the photoluminescence intensity of MoS<sub>2</sub> with thickness.<sup>(32)</sup> Furthermore, the magnetic force microscopy (MFM) data also show that the magnetic property of MoS<sub>2</sub> depends on the number of layers.<sup>(33)</sup> The calculated spin density distribution in the MoS<sub>2</sub>/CdS heterostructure is exhibited in panels a and b of Figure 3, and that of the Mo atom in the interfacial MoS<sub>2</sub> monolayer is displayed in Figure 3c.

Clearly, there is significant spin density only in the interfacial MoS<sub>2</sub> monolayer ([Figure 3a,b](#)), where the spin density distribution of Mo is similar to that of the d<sub>x<sup>2</sup>-y<sup>2</sup></sub> orbital ([Figure 3c](#)). The results indicate that the major contribution comes from Mo d orbitals. This is because the Fermi level is raised above the bottom of the conduction Mo d<sub>x<sup>2</sup>-y<sup>2</sup></sub> and d<sub>xy</sub> bands in the interfacial monolayer, as revealed by calculated Mo-decomposed spin-resolved DOSs shown in [Figure 3d](#) (see also [Figure S5](#)). Interestingly, the calculated spin-resolved DOS curves show that the local DOS of the Cd atoms on the interfacial Cd monolayer is also spin-polarized ([Figure S6](#)), because of the magnetic proximity effect on the Cd atoms by the magnetic Mo atoms via the S atoms across the interface. For example, the spin polarizations for the S atoms on the interface S monolayer and the Cd atoms on the Cd monolayer next to the interface are 20% (S<sub>M1</sub>) and 16% (Cd<sub>1</sub>), respectively (see [Figure 4b](#) and also [Figures S6 and S7](#)).

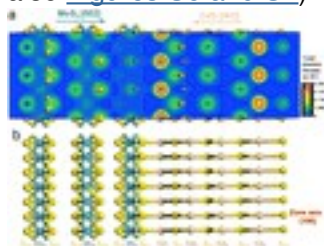


Figure 4. Electron density distribution of the MoS<sub>2</sub>/CdS heterostructure. (a) Total electron density distribution of the MoS<sub>2</sub>/CdS heterostructure shown with the isosurface (blue line, isovalue of 0.13876 e/Å<sup>3</sup>). (b) Atomic model of the MoS<sub>2</sub>/CdS heterostructure with the [100] zone axis.

[Figure 4a](#) shows the calculated charge density distribution in the MoS<sub>2</sub>/CdS heterostructure as modeled by the atomic model shown in [Figure 3b](#). For the sake of discussion, the different atomic locations in the vicinity of the MoS<sub>2</sub>/CdS interface are labeled, as shown in [Figure 4b](#). The charge density distribution in the region from the S<sub>M4</sub> to Cd<sub>2</sub> atom layer is rather flat, having a similar isosurface with an isovalue of 0.139 e/Å<sup>3</sup>. Inside the region, the electron density in some areas is higher than the isovalue, indicating some bonding between the S and Cd atoms across the MoS<sub>2</sub>/CdS interface. This covalent bonding could be attributed to the similar electronegativities of the Mo (1.3) and Cd (1.5) atoms. Remarkably, the calculated DOS curves ([Figure S5](#)) show that this covalent bonding causes some charge transfer from the Mo d bands in the outer MoS<sub>2</sub> monolayer (Mo<sub>3</sub>) to the Mo d bands in the interfacial MoS<sub>2</sub> monolayer (Mo<sub>1</sub>), leading to the partial occupation of the Mo d<sub>x<sup>2</sup>-y<sup>2</sup></sub> and d<sub>xy</sub> dominant bands of the Mo<sub>1</sub> atoms. This charge transfer is also seen from the calculated numbers of valence electrons on the Mo<sub>1</sub> (6.38), Mo<sub>2</sub> (6.17), and Mo<sub>3</sub> (6.02) atoms ([Table S1](#)). As a result, the strong exchange interaction among the Mo d electrons then gives rise to the

formation of the Mo<sub>1</sub> spin magnetic moment, and hence the ferromagnetic MoS<sub>2</sub> monolayer next to the MoS<sub>2</sub>/CdS interface.

## Conclusions

In summary, magnetic MoS<sub>2</sub> thin films have been grown on CdS NWs by cation exchange at room temperature. The magnetism in the MoS<sub>2</sub>/CdS heterostructure was shown to stem from the ferromagnetic MoS<sub>2</sub> monolayer next to the MoS<sub>2</sub>/CdS interface by first-principles DFT-GGA calculations. The ferromagnetism was attributed to the partial occupation of the Mo d<sub>x<sup>2</sup>-y<sup>2</sup></sub>/d<sub>xy</sub> conduction band in the interfacial MoS<sub>2</sub> monolayer caused by the mixed covalent–ionic bonding among the MoS<sub>2</sub> and CdS monolayers near the MoS<sub>2</sub>/CdS interface. This work thus offers a new paradigm for fabrication of the transition metal dichalcogenide-based magnetic semiconductor multilayers for applications in spintronic devices such as tunnel junctions with high magnetoresistance.

## Supporting Information

The Supporting Information is available free of charge on the [ACS Publications website](https://pubs.acs.org) at DOI: [10.1021/acs.jpcc.6b07679](https://doi.org/10.1021/acs.jpcc.6b07679).

- Additional figures displaying measured Raman spectra, SEM images and hysteresis loops, and calculated atom- and orbital-decomposed densities of states and additional tables listing calculated occupation numbers of atomic orbitals and structural parameters of the atomic model adopted in the SEM image simulations and DFT-GGA calculations ([PDF](#))
- **PDF**
  - [jp6b07679\\_si\\_001.pdf \(910.93 kB\)](#)

## Magnetic MoS<sub>2</sub> Interface Monolayer on a CdS Nanowire by Cation Exchange

[figshare](#)

Share [Download](#)

The authors declare no competing financial interest.

- 

## Acknowledgment

We thank K. L. Lin at National Nano Device Laboratories for a discussion of the experimental results. The authors are grateful for the research support from the Ministry of Science and Technology of R.O.C. under Projects MOST 103-2221-E-007-003 and MOST 104-2112-M-002-002-MY3, the Academia Sinica Thematic Research Program, and the National Center of Theoretical Sciences.

- [Reference QuickView](#)
- 

## References

This article references 33 other publications.

1. [1.](#)

Wang, Q. H.; Kalantar-Zadeh, K.; Kis, A.; Coleman, J. N.; Strano, M. S. Electronics and Optoelectronics of Two-dimensional Transition Metal Dichalcogenides *Nat. Nanotechnol.* **2012**, 7, 699– 712 DOI: 10.1038/nnano.2012.193

[\[Crossref\]](#), [\[PubMed\]](#), [\[CAS\]](#)

2. [2.](#)

Johari, P.; Shenoy, V. B. Tuning the Electronic Properties of Semiconducting Transition Metal Dichalcogenides by Applying Mechanical Strains *ACS Nano* **2012**, 6, 5449– 5456 DOI: 10.1021/nn301320r

[\[ACS Full Text\]](#) , [\[CAS\]](#)

3. [3.](#)

Hong, X.; Liu, J.; Zheng, B.; Huang, X.; Zhang, X.; Tan, C.; Chen, J.; Fan, Z.; Zhang, H. A Universal Method for Preparation of Noble Metal Nanoparticle-decorated Transition Metal Dichalcogenide Nanobelts *Adv. Mater.* **2014**, 26, 6250– 6254 DOI: 10.1002/adma.201402063

[\[Crossref\]](#), [\[PubMed\]](#), [\[CAS\]](#)

4. [4.](#)

Fang, H.; Tosun, M.; Seol, G.; Chang, T. C.; Takei, K.; Guo, J.; Javey, A. Degenerate n-doping of Few-layer Transition Metal Dichalcogenides by Potassium *Nano Lett.* **2013**, 13, 1991– 1995 DOI: 10.1021/nl400044m

[\[ACS Full Text\]](#), [\[CAS\]](#)

5. [5.](#)

Radisavljevic, B.; Radenovic, A.; Brivio, J.; Giacometti, V.; Kis, A. Single-layer MoS<sub>2</sub> Transistors *Nat. Nanotechnol.* **2011**, 6, 147– 150 DOI: 10.1038/nnano.2010.279

[\[Crossref\]](#), [\[PubMed\]](#), [\[CAS\]](#)

6. [6.](#)

Splendiani, A.; Sun, L.; Zhang, Y.; Li, T.; Kim, J.; Chim, C. Y.; Galli, G.; Wang, F. Emerging Photoluminescence in Monolayer MoS<sub>2</sub> *Nano Lett.* **2010**, 10, 1271– 1275 DOI: 10.1021/nl903868w

[\[ACS Full Text\]](#), [\[CAS\]](#)

7. [7.](#)

Li, Y.; Wang, H.; Xie, L.; Liang, Y.; Hong, G.; Dai, H. MoS<sub>2</sub> Nanoparticles Grown on Graphene: an Advanced Catalyst for the Hydrogen Evolution Reaction *J. Am. Chem. Soc.* **2011**, 133, 7296– 7299 DOI: 10.1021/ja201269b

[\[ACS Full Text\]](#), [\[CAS\]](#)

8. [8.](#)

Lee, K.; Kim, H. Y.; Lotya, M.; Coleman, J. N.; Kim, G. T.; Duesberg, G. S. Electrical Characteristics of Molybdenum Disulfide Flakes Produced by Liquid Exfoliation *Adv. Mater.* **2011**, 23, 4178– 4182 DOI: 10.1002/adma.201101013

[\[Crossref\]](#), [\[PubMed\]](#), [\[CAS\]](#)

9. [9.](#)

Liu, N.; Kim, P.; Kim, J. H.; Ye, J. H.; Kim, S.; Lee, C. J. Large-area Atomically Thin MoS<sub>2</sub> Nanosheets Prepared Using Electrochemical Exfoliation *ACS Nano* **2014**, 8, 6902– 6910 DOI: 10.1021/nn5016242

[\[ACS Full Text\]](#), [\[CAS\]](#)

10. [10.](#)

Yang, L.; Wang, S.; Mao, J.; Deng, J.; Gao, Q.; Tang, Y.; Schmidt, O. G. Hierarchical MoS<sub>2</sub>/polyaniline Nanowires with Excellent Electrochemical Performance for Lithium-ion Batteries *Adv. Mater.* **2013**, 25, 1180– 1184 DOI: 10.1002/adma.201203999

[\[Crossref\]](#), [\[PubMed\]](#), [\[CAS\]](#)

11. [11.](#)

Wu, S.; Ross, J. S.; Liu, G.

B.; Aivazian, G.; Jones, A.; Fei, Z.; Zhu, W.; Xiao, D.; Yao, W.; Cobden, D.; Xu, X. Electrical Tuning of Valley Magnetic Moment Through Symmetry Control in Bilayer MoS<sub>2</sub> *Nat. Phys.* **2013**, 9, 149– 153 DOI: 10.1038/nphys2524

[\[Crossref\]](#), [\[CAS\]](#)

12. [12.](#)

Li, Y.; Zhou, Z.; Zhang, S.; Chen, Z. MoS<sub>2</sub> nanoribbons: High Stability and Unusual Electronic and Magnetic Properties *J. Am. Chem. Soc.* **2008**, 130, 16739– 16744 DOI: 10.1021/ja805545x

[\[ACS Full Text\]](#) , [\[CAS\]](#)

13. [13.](#)

Tongay, S.; Varnoosfaderani, S. S.; Appleton, B. R.; Wu, J.; Hebard, A. F. Magnetic Properties of MoS<sub>2</sub>: Existence of Ferromagnetism *Appl. Phys. Lett.* **2012**, 101, 123105 DOI: 10.1063/1.4753797

[\[Crossref\]](#), [\[CAS\]](#)

14. [14.](#)

Zhang, J.; Soon, J. M.; Loh, K. P.; Yin, J.; Ding, J.; Sullivan, M. B.; Wu, P. Magnetic Molybdenum Disulfide Nanosheet Films *Nano Lett.* **2007**, 7, 2370– 2376 DOI: 10.1021/nl071016r

[\[ACS Full Text\]](#) , [\[CAS\]](#)

15. [15.](#)

Pan, H.; Zhang, Y. W. Edge-dependent Structural, Electronic and Magnetic Properties of MoS<sub>2</sub> Nanoribbons *J. Mater. Chem.* **2012**, 22, 7280– 7290 DOI: 10.1039/c2jm15906f

[\[Crossref\]](#), [\[CAS\]](#)

16. [16.](#)

Feng, N.; Mi, W.; Cheng, Y.; Guo, Z.; Schwingenschlögl, U.; Bai, H. Magnetism by Interfacial Hybridization and p-type Doping of MoS<sub>2</sub> in Fe<sub>4</sub>N/MoS<sub>2</sub> Superlattices: A First-principles Study *ACS Appl. Mater. Interfaces* **2014**, 6, 4587– 4594 DOI: 10.1021/am500754p

[\[ACS Full Text\]](#) , [\[CAS\]](#)

17. [17.](#)

Chang, L. T.; Wang, C. Y.; Tang, J.; Nie, T.; Jiang, W.; Chu, C. P.; Arafin, S.; He, L.; Afsal, M.; Chen, L. J. Electric-field Control of Ferromagnetism in Mn-doped ZnO Nanowires *Nano Lett.* **2014**, *14*, 1823– 1829 DOI: 10.1021/nl404464q

[[ACS Full Text](#) ], [[CAS](#)]

18. [18.](#)

Tang, J.; Wang, C. Y.; Chang, L. T.; Fan, Y.; Nie, T.; Chan, M.; Jiang, W.; Chen, Y. T.; Yang, H. J.; Tuan, H. Y. Electrical Spin Injection and Detection in  $\text{Mn}_3\text{Ge}_3/\text{Ge}/\text{Mn}_3\text{Ge}_3$  Nanowire Transistors *Nano Lett.* **2013**, *13*, 4036– 4043 DOI: 10.1021/nl401238p

[[ACS Full Text](#) ], [[CAS](#)]

19. [19.](#)

Koo, H. C.; Kwon, J. H.; Eom, J.; Chang, J.; Han, S. H.; Johnson, M. Control of Spin Precession in a Spin-injected Field Effect Transistor *Science* **2009**, *325*, 1515– 1518 DOI: 10.1126/science.1173667

[[Crossref](#)], [[PubMed](#)], [[CAS](#)]

20. [20.](#)

Chuang, P.; Ho, S. C.; Smith, L. W.; Sfigakis, F.; Pepper, M.; Chen, C. H.; Fan, J. C.; Griffiths, J. P.; Farrer, I.; Beere, H. E.; Jones, G. A. C.; Ritchie, D. A.; Chen, T.-M. All-electric All-semiconductor Spin Field-effect Transistors *Nat. Nanotechnol.* **2014**, *10*, 35– 39 DOI: 10.1038/nnano.2014.296

[[Crossref](#)], [[PubMed](#)]

21. [21.](#)

Tan, C. S.; Hsiao, C. H.; Wang, S. C.; Liu, P. H.; Lu, M. Y.; Huang, M. H.; Ouyang, H.; Chen, L. J. Sequential Cation Exchange Generated Superlattice Nanowires Forming Multiple p–n Heterojunctions *ACS Nano* **2014**, *8*, 9422– 9426 DOI: 10.1021/nn5035247

[[ACS Full Text](#) ], [[CAS](#)]

22. [22.](#)

Koch, C. T. Determination of Core Structure Periodicity and Point Defect Density Along Dislocations. Ph.D. Thesis, Arizona State University, Tempe, AZ, **2002**.

23. [23.](#)

Perdew, J. P.; Burke, K.; Ernzerhof, M. Generalized Gradient Approximation Made Simple *Phys. Rev. Lett.* **1996**, *77*, 3865 DOI: 10.1103/PhysRevLett.77.3865

[[Crossref](#)], [[PubMed](#)], [[CAS](#)]

24. [24.](#)  
Beberwyck, B. J.; Alivisatos, A. P. Ion Exchange Synthesis of III–V nanocrystals *J. Am. Chem. Soc.* **2012**, 134, 19977– 19980 DOI: 10.1021/ja309416c  
[\[ACS Full Text\]](#), [\[CAS\]](#)
25. [25.](#)  
Gupta, S.; Kershaw, S. V.; Rogach, A. L. Ion Exchange in Colloidal Nanocrystals *Adv. Mater.* **2013**, 25, 6923– 6944 DOI: 10.1002/adma.201302400  
[\[Crossref\]](#), [\[PubMed\]](#), [\[CAS\]](#)
26. [26.](#)  
Kim, M.; Cahill, J. F.; Fei, H.; Prather, K. A.; Cohen, S. M. Postsynthetic Ligand and Cation Exchange in Robust Metal–organic Frameworks *J. Am. Chem. Soc.* **2012**, 134, 18082– 18088 DOI: 10.1021/ja3079219  
[\[ACS Full Text\]](#), [\[CAS\]](#)
27. [27.](#)  
Tang, J.; Huo, Z.; Brittman, S.; Gao, H.; Yang, P. Solution-processed Core-shell Nanowires for Efficient Photovoltaic Cells *Nat. Nanotechnol.* **2011**, 6, 568– 572 DOI: 10.1038/nnano.2011.139  
[\[Crossref\]](#), [\[PubMed\]](#), [\[CAS\]](#)
28. [28.](#)  
Tan, C. S.; Chen, H. Y.; Chen, H. S.; Gwo, S.; Chen, L. J. Intermediates in the Cation Reactions in Solution Probed by an in situ Surface Enhanced Raman Scattering Method *Sci. Rep.* **2015**, 5, 13759 DOI: 10.1038/srep13759  
[\[Crossref\]](#), [\[PubMed\]](#), [\[CAS\]](#)
29. [29.](#)  
Lu, K. C.; Wu, W. W.; Wu, H. W.; Tanner, C. M.; Chang, J. P.; Chen, L. J.; Tu, K. N. In-situ Control of Atomic-scale Si Layer with Huge Strain in the Nano-heterostructure NiSi/Si/NiSi Through Point Contact Reaction *Nano Lett.* **2007**, 7, 2389– 2394 DOI: 10.1021/nl071046u  
[\[ACS Full Text\]](#), [\[CAS\]](#)
30. [30.](#)  
Kästner, G.; Goesele, U. Stress and Dislocations at Cross-sectional Heterojunctions in a Cylindrical Nanowire *Philos. Mag.* **2004**, 84, 3803– 3824 DOI: 10.1080/1478643042000281389  
[\[Crossref\]](#)



31. [31.](#)

Wang, C. Y.; Guo, G. Y. Nonlinear Optical Properties of Transition Metal Dichalcogenide  $\text{MX}_2$  (M= Mo, W; X= S, Se) Monolayers and Trilayers from First-principles Calculations *J. Phys. Chem. C* **2015**, 119, 13268–13276 DOI: 10.1021/acs.jpcc.5b01866

[\[ACS Full Text\]](#) 

32. [32.](#)

Li, H.; Zhang, Q.; Yap, C. C. R.; Tay, B. K.; Edwin, T. H. T.; Olivier, A.; Baillargeat, D. From Bulk to Monolayer  $\text{MoS}_2$ : Evolution of Raman Scattering *Adv. Funct. Mater.* **2012**, 22, 1385– 1390 DOI: 10.1002/adfm.201102111

[\[Crossref\]](#), [\[CAS\]](#)

33. [33.](#)

Li, H.; Qi, X.; Wu, J.; Zeng, Z.; Wei, J.; Zhang, H. Investigation of  $\text{MoS}_2$  and Graphene Nanosheets by Magnetic Force Microscopy *ACS Nano* **2013**, 7, 2842– 2849 DOI: 10.1021/nn400443u

[\[ACS Full Text\]](#) , [\[CAS\]](#)